Predictive Modeling for Glass-Side Laser Scribing of Thin Film Photovoltaic Cells

Hongliang Wang[a,*], Shan-Ting Hsu[a], Huade Tan[a], Y. Lawrence Yao[a],

Hongqiang Chen[b], Magdi N. Azer[b]

[a] Department of Mechanical Engineering, Columbia University, New York, NY, USA

[b] Laser & Metrology System Lab, GE Global Research, Niskayuna, NY, USA

[*] Corresponding author. Tel.: +1 212 666 2393; e-mail address: hw2288@columbia.edu

Abstract

Laser scribing of multilayer-thin-film solar cells is an important process for producing integrated serial interconnection of mini-modules, used to reduce photocurrent and resistance losses in a large-area solar cell. Quality of such scribing contributes to the overall quality and efficiency of the solar cell and therefore predictive capabilities of the process are essential. Limited numerical work has been performed in predicting the thin film laser removal processes. In this study, a fully-coupled multilayer thermal and mechanical finite element model is developed to analyze the laser-induced spatio-temporal temperature and thermal stress responsible for SnO_2:F film removal. A plasma expansion induced pressure model is also investigated to simulate the non-thermal film removal of CdTe due to the micro-explosion process. Corresponding experiments of SnO_2:F films on glass substrates by 1064nm ns laser irradiation show a similar removal process to that predicted in the simulation. Differences between the model and experimental results are discussed and future model refinements are proposed. Both simulation and experimental results from glass-side laser scribing show clean film removal with minimum thermal effects indicating minimal changes to material electrical properties.

Keywords: Modeling, laser scribing, multilayer thin films, SnO_2:F, CdTe, solar cell

1. Introduction

Thin-film solar cell technology promises to achieve a significant cost reduction in materials, by adopting large area deposition capability, and the use of cheap and flexible substrates. Typical thin film solar cells used in terrestrial PV (photovoltaic) applications consist of back contact, absorber and front contact films. CdTe (Cadmium telluride) is the dominant absorber material in recent years because of its attractive price and stable performance at high temperatures [1-2]. The efficiency of thin-film solar panels, however, is hampered by resistive losses in the module proportional to the square of the photocurrent. In practice, photocurrent is decreased by scribing the solar module into a large number (between 100 and 200) mini-modules and connecting them in series to create high-voltage, low-current devices [3]. Since each layer in the solar module must be scribed after deposition, scribing is performed in 3 steps – Patterns 1, 2 and 3 (P1, P2 and P3) processes, which are also used in the commercial production of a-Si:H (hydrogenated amorphous silicon) and CI(G)S (copper indium gallium selenide) based thin film solar cell fabrications [4-6]. Laser scribing offers narrower scribe widths and less damage in the surrounding material compared to the mechanical scribing. However, laser scribing has been shown to leave a heat-affected zone around the scribe, which causes undesirably poor isolation between cells and low shunt resistance. Laser scribing has also been shown to leave high protruded ridges along the edge of the scribe line, contributing to electrical shorts [4]. While scribing reduces resistive losses by decreasing photocurrent, it also forms dead zones between P1 and P3 slots, which contribute to reductions in module efficiency [7].

In order to decrease the thermal effect of laser irradiation during processing, the use of ultrashort pulsed lasers, such as picosecond and femtosecond lasers, are being investigation for scribing processes [8-9]. These lasers are complex and expensive, and regardless of pulse duration, material melting cannot be totally eliminated [5]. Glass side laser processing [10-11] has been shown to be more efficient than film side processing with reduced thermal effect. Film side laser scribing is governed by heating, melting and vaporizing of selective films, while glass side laser scribing is a thermal-mechanical process which involves stress induced material failure and removal rather than vaporization. The mechanical fracture and removal of film material during glass side scribing is commonly referred to as lift off or micro-explosion processing. During micro-explosion processing, the laser irradiates through the transparent substrate and is fully absorbed in a very thin layer of film at the interface. High pressure plasma is generated and expanded in the film. The plasma punches through the solid film above and the material is removed mechanically [12]. Micro-explosion processing is pronounced when the laser material penetration depth is much shallower than the film thickness. One example is that of CdTe irradiated with a green laser at a wavelength of 532nm. Laser energy is mainly absorbed at the CdTe/substrate interface. High pressure plasma is generated and lifts off the solid film above. For front contact films made by transparent conducting oxide (TCO) materials, such as ITO (indium tin oxide) and SnO_2:F (fluorine-doped tin dioxide), penetration depths exceed that of the film thicknesses, and the micro-explosion process cannot occur during laser scribing. Because of this effect it is difficult to scribe the TCO layers with low thermal effects using nanosecond (ns) lasers.

While glass-side laser scribing has led to improved scribe quality over competing methods, defects such as irregular scribe geometry, heat-affected zones and micro cracks that lead to

decreased module efficiency are still introduced [13-14]. The physical phenomena responsible for film removal during laser scribing and their effect on scribe quality are not well known. Development of simulation capabilities will enable the fundamental understanding of the physical mechanisms and optimize the scribing processes instead of relying on trial-and-error experiments. To date, only rudimentary modeling efforts have been made, offering no predictive or optimization capabilities. Bovatsek et al. [6] developed a simple, one-dimensional thermal model to estimate the through thickness temperature variation of a-Si:H based thin film solar cells by ns laser pulse irradiated from the glass side, and estimated the thermal stress as that of an expanding plate with fixed edges heated by a laser. While this model shows the formation of thermal stresses, caused by the laser fluence lower than the melting threshold, can exceed the material's compressive yield stress, it offers no predictive capabilities of the scribe geometry due to the lack of spatial and temporal resolution. There is also limited simulation effort on micro-explosion processes.

Based on the current thin-film solar cell technology, a 1% increase in efficiency from improved scribe quality equates to roughly a 10% reduction cost. Therefore, numerical models of laser scribing processes that predict scribing width, cleanliness and thermal effect are important for the cost reduction of thin film solar cells. In this paper, two-dimensional numerical models are developed to simulate SnO_2:F and CdTe film removal via a fully-coupled thermo-mechanical stress analysis and micro-explosion processes, respectively. Brittle material failure and traction stresses at the film/substrate interface are incorporated to determine film fracture and delamination. Simulation results of SnO_2:F film removal from glass substrate are experimentally validated by glass side laser scribing. The scribe geometry and quality are characterized and

studied by scanning electron microscopy (SEM), optical profilometry, and energy-dispersive x-ray spectroscopy (EDX).

2. Background

Because the entire layer of SnO_2:F can absorb the laser energy uniformly due to its high optical penetration depth compared to its thickness (400nm), SnO_2:F is usually removed by laser ablation which results in a heat-affected zone. Here, a film removal process of SnO_2:F with low laser fluences (less than melting threshold) is investigated. It is found that the SnO_2:F film is removed by the thermal-induced stress. CdTe, which has a lower optical penetration depth than its thickness (2μm), it is commonly removed by micro-explosion process. Because the CdTe film is thicker than the SnO_2:F film, it is difficult to thermally ablate with a single pulse. High-pressure plasma is generated at the film/substrate interface while applying laser from the glass side, and the solid film above is lifted off during plasma expansion. CdTe film undergoes brittle material cracking during the plasma expansion, and the material at the plasma boundaries is delaminated simultaneously. Film delamination is analyzed by the traction separation mechanism at the interface, which is implemented using cohesive elements in the simulation.

2.1 Thermal Stress and Brittle Failure Analysis

During laser irradiation, the spatial and temporal distribution of temperature is governed by the heat equation

$$\rho C_P \left(\partial T / \partial t\right) = \nabla \cdot \left(k \nabla T\right) + q\left(r, z, t\right) \tag{1}$$

where ρ, C_p, T, t and k are density, specific heat, temperature, time and thermal conductivity; r and z are the radial distance to the laser beam center and film thickness, respectively; laser power density $q(r,z,t)$ represented temporal and spatial distribution within the film is given as

$$q(r,z,t) = q_0 \cdot exp(-\kappa z) \cdot exp\left[-2r^2 / R_0^2\right] \cdot exp\left[-4ln2(t/t_p - 1)^2\right] \quad (2)$$

where q_0, κ, R_0 and t_p are the peak power density, absorption coefficient, beam radius and pulse width. When a structure is mechanically constrained, thermal stresses are induced by thermal expansion, as determined by the Hooke's Law, $\varepsilon = \alpha \Delta T$, where α is thermal expansion coefficient and ΔT is the temperature change. Because the thermal and mechanical response of the material is interpedent, a fully-coupled thermo-mechanical analysis, is implemented.

SnO_2:F and CdTe are considered as brittle materials and a precise failure criterion, which captures failure of a brittle material by both tensile and compressive stresses, can be provided by the Coulomb-Mohr criterion, written as [15]

$$\begin{cases} \sigma_1 > R_r \, or \, \sigma_2 > R_r, \, if \;\; \sigma_1 \, and \, \sigma_2 > 0; & \sigma_1 < -R_c \, or \, \sigma_2 < -R_c, \, if \;\; \sigma_1 \, and \, \sigma_2 < 0 \\ \sigma_1 / R_r + \sigma_2 / -R_c > 1, \, if \;\; \sigma_1 > 0 \, and \, \sigma_2 < 0; & \sigma_1 / -R_c + \sigma_2 / R_r > 1, \, if \;\; \sigma_1 < 0 \, and \, \sigma_2 > 0 \end{cases} \quad (3)$$

where σ_1 and σ_2 are the principal stresses, and R_t and R_c are the tensile and compressive failure strengths, respectively. When the principal stress of the brittle material elements exceed the Coulomb-Mohr criterion, the elements fail and cannot carry stresses any longer, and are removed from the calculation.

2.2 Micro-Explosion Analysis

When a target, i.e. CdTe, is irradiated by an intense laser pulse, due to its small optical penetration depth, the laser energy absorbed at the CdTe/substrate interface ionizes the material

into plasma. Since the plasma is confined by the film and substrate, the solid CdTe film is lifted off during the plasma expansion, this process is known as the micro-explosion or lift-off mechanism [12]. The confined pressure induced by laser-produced plasma is estimated by Fabbro et al. [16], which assumes a constant fraction α of internal energy goes into the thermal energy of the plasma while the rest (1- α) is used for ionization of the gas. The relationship between plasma pressure *P(t)* and plasma thickness *L(t)* can be derived from [17]

$$\frac{dL(t)}{dt} = \frac{2P(t)}{Z} \tag{4}$$

$$\left(\frac{Z}{2} + \frac{3Z}{4\alpha}\right)\left(\frac{dL(t)}{dt}\right)^2 + \frac{3Z}{4\alpha}L(t)\frac{d^2L(t)}{dt^2} = AI(t) \tag{5}$$

where Z is the impedance of shock wave caused by the plasma expansion, t is time, *I(t)* is the incident laser intensity and A is absorption coefficient of plasma. It is also assumed that plasma pressure follows a Gaussian spatial distribution with its $1/e^2$ radius proportional to the $1/e^2$ radius of the laser beam. The pressure is expressed as a function of space and time as $P(r,t) = P(t) \cdot exp\left[-r^2 / 2R_0^2\right]$, where R_0 is the laser beam radius.

2.3 Traction Separation Analysis

Because laser induced plasma expansion at the CdTe film/substrate interface can delaminate the film from the substrate, traction separation behaviors at the interface are considered using cohesive elements. The traction stress vector, ***t***, consists of two components t_u and t_v, which represent the normal and shear tractions. Corresponding displacements are δ_u and δ_v, and the strains are obtained by $\varepsilon_u = \delta_u / T_0$, $\varepsilon_v = \delta_v / T_0$, where T_0 is the original thickness of the interfacial elements. Before interface damage occurs, the relationship between the traction stress and strain is written as

$$\boldsymbol{t} = \begin{Bmatrix} t_u \\ t_v \end{Bmatrix} = \begin{bmatrix} K_{uu} & K_{uv} \\ K_{uv} & K_{vv} \end{bmatrix} \begin{Bmatrix} \varepsilon_u \\ \varepsilon_v \end{Bmatrix} = \boldsymbol{K}\varepsilon \tag{6}$$

where K_{uu} and K_{vv} are the stiffness in the principal directions, while K_{uv} is the stiffness in the shear direction. The CdTe/substrate traction separation law states that the traction stress depends linearly on the strain, but starts decreasing once the quadratic nominal stress ratio reaches one [18],

$$\left\{\frac{\langle t_u \rangle}{t_u^0}\right\}^2 + \left\{\frac{t_v}{t_v^0}\right\}^2 = 1 \tag{7}$$

where material constants t_u^0 and t_v^0 are the critical values in the normal and shear directions, where the interface damage initiates. The value of $\langle t_u \rangle$ is 0 if $t_u < 0$ and t_u if $t_u > 0$, because a purely compressive stress does not initiate damage. When the stress criterion is reached, the traction stresses decrease as [19]

$$\bar{t}_u = \begin{cases} (1-D)t_u, & t_u > 0 \\ t_u, & t_u \le 0 \end{cases}, \quad \bar{t}_v = (1-D)t_v \tag{8}$$

where the scalar damage variable, D, increases from 0 to 1 upon further loading after the initiation of damage. $\bar{t}_u$ and $\bar{t}_v$ are the stress components as a result of damage evolution. The scalar damage variable D is given as [19]

$$D = \frac{\delta_m^f \left(\delta_m^{max} - \delta_m^o\right)}{\delta_m^{max}\left(\delta_m^f - \delta_m^o\right)} \tag{9}$$

where δ_m is the effective displacement defined as $\delta_m = \sqrt{\langle \delta_u \rangle^2 + \delta_v^2}$, and the superscripts *max*, *o*, and *f* denote the maximum, initiation, and failure points. Eqs. (7) to (9) describe the failure behavior of the cohesive elements used in simulation and film delamination occurs when the effective displacement of the material at the interface reaches the critical value, δ_m^f.

The above analyses are carried out through a finite element method. Explicit time-stepping scheme is used for modeling this laser-induced highly dynamic process. A user-defined material property subroutine VUMAT is developed for identification of the material removal based on the criteria mentioned above.

3. Experimental Setup

The front contact layers, Polycrystalline TCO (SnO_2:F) material, were deposited on 3.2mm-thick soda-lime glass substrates using the chemical vapor deposition method at 1100ºF. The deposited SnO_2:F film thickness was measured to be 400nm by ellipsometry.

Laser scribing was carried out on the multilayer thin-film samples with a Q-switched Nd:YAG laser. The laser system delivered 50 ns pulses with a wavelength of 1064nm and a repetition rate of 1kHz. The SnO_2:F films were cleaned with acetone in an ultrasonic cleaner for 5 minutes and then rinsed with methanol and distilled water prior to laser processing. The sample, mounted on a three-axis translation stage, was irradiated by laser pulses focused by a 20mm effective-focal-length objective lens. The laser focal plane was placed at the SnO_2:F/glass interface with a circular 10μm in diameter beam spot. Both glass side-scribing and film-side scribing were conducted.

Laser treated samples were observed through SEM, and scribe profiles were measured by optical profilometry. The chemical components of laser processed samples were investigated by EDX to estimate the scribing quality.

4. **Results and Discussion**

4.1 **Simulation on SnO_2:F Film Removal by Thermal Stress**

The schematic of glass-side laser scribing of SnO_2:F and CdTe in both simulation and experiments is illustrated in Fig. 1. The SnO_2:F film thickness is 400nm, the glass substrate is 50μm thick, and the width of the model is 100μm in the simulation. A 50-ns pulse duration laser with a wavelength of 1064nm is used for SnO_2:F film scribing, a wavelength of 532nm is used for CdTe film scribing. The material properties of SnO_2:F, CdTe, and the soda-lime glass substrate used in the simulation are listed in Table 1.

SnO_2:F is usually scribed through thermal ablation, however, a large area of heat-affected zone is always introduced. Here, in order to minimize the thermal effect, a simulation investigation of SnO_2:F film removal with a laser fluence lower than the melting threshold is carried out. By considering the energy loss due to the absorption and reflection by the glass substrate as well as the reflection by SnO_2:F/glass interface, the laser energy source in the SnO_2:F layer is written as [6]

$$E(r,z,t) = \alpha_f (1-R_f)(1-R_g-A_g) I(r,z,t) e^{-\alpha_f (z-T_g)} \tag{10}$$

where *I(r,z,t)* is the incident laser pulse energy. R_f and α_f are the reflectivity and absorption coefficient of SnO_2:F. R_g, A_g and T_g are the reflectivity, absorption and thickness of glass substrate. The results of thermal analysis are shown in Fig. 2. In the simulation, the SnO_2:F film is treated under a fluence of 3J/cm^2, which is less than the melting threshold (~4J/cm^2 for 1064nm @ 70ns) [4], and laser is irradiated from the glass side. The highest temperature of SnO_2:F during the simulation history is 1848K, which is less than the melting point of 1903K. The large penetration depth in SnO_2:F, around 2μm at 1064nm, causes a uniform temperature distribution along the film's thickness.

The fully-coupled analysis considers the simultaneous dependence between the variations of temperature, thermal stress and film deformation. In addition, the brittle failure analysis is implemented in order to simulate the film removal caused by the thermal stress. Fig. 3 shows a snapshot of the film removal process at 38ns. It can be seen that a 2μm opening has been generated at this moment since the elements have experienced the compressive principal stresses that are adequate to meet the Coulomb-Mohr criterion. While the absorption coefficient of SnO_2:F is much larger than that of glass, during the 50ns laser heating time, the SnO_2:F film expands much faster than that of glass, which results in a compressive stress in the film due to the confinement of the substrate. Elements are removed when the compressive stresses meet Coulomb-Mohr criterion. The evolution of the principal stress and the heat flux in an element at the center of SnO_2:F film are shown in Fig. 4. It can be observed that compressive stress is dominant in S_{11}, due to the discrepancy of the thermal expansions between the SnO_2:F film and glass substrate. Before element failure occurs, the compressive principal stress keeps increasing. Once the material fails, the element loses its ability to carry stress or heat which affects the subsequent simulation step in the fully-coupled analysis. Fig. 5 shows the final results of complete SnO_2:F film removal irradiated at a fluence $3J/cm^2$ at 200ns. A clean film removal is obtained with an opening of 8.3μm. Since phase change is not considered in the simulation, thermally induced compressive stress in the film is dominant during the film removal process.

When the film is irradiated at a lower fluence, $1J/cm^2$, the compressive stress inside the film is not adequate enough to cause the film fracture. Tension needs to be considered. In Fig. 6, the temperature history output shows that the glass temperature increase has a time delay compared with that of SnO_2:F. This indicates that part of the heat transfers to the glass after the fast laser heating of the film, which leads to the transition from compression to tension in the film. The

expansion coefficient of glass is twice of that of SnO_2:F. The temperature change of glass is greater than SnO_2:F for a unit energy input. Thus, glass expands more than the film while heat is conducted from the film to the substrate. This leads to the decrease of compressive stress, and a transition to tensile stress when the glass expansion exceeds that of the film. The time history evolution of principal stress in a deleted element under a laser irradiation with a fluence of $1J/cm^2$ is shown in Fig. 6. A clear transition between compressive and tensile stresses (S_{11}) is observed and the element is removed when the Coulomb-Mohr criterion is met. The effect of tension is neglected when the film is removed by compressive stress at higher fluences. The reason is because the elements around the scribe removed during the laser irradiation are free of confinement in r direction, which eliminates the subsequent dominant tensile stress (S_{11}). Because the film removal occurs during the laser heating time when compressive stress is dominant, the heated film is removed from the calculation before transferring the heat to the substrate; therefore, the glass thermal expansion will be much smaller and the tension is too small to fracture the rest solid film. At low fluences where compressive stress cannot lead to film removal, tensile stresses can be dominant for the removal.

A comparison of experimental and simulation results are shown in Fig. 7. It is observed that the scribe widths obtained from the simulation are close to the experimental results and both show a linearly increasing relationship between scribe width and laser fluence. Simulation results show that film removal is complete for all conditions; however, the experimental results depict that the films are partially removed in depth and the removal depths vary linearly with increasing laser fluence. Discrepancies between the simulation and experimental results are caused by neglecting the effect of the interface. As shown in the simulation, the temperature and stress distributions along the thickness direction are uniform due to the large laser penetration depth. However, the

impurities or defects induced during the deposition process can absorb a fraction of laser energy and less energy is absorbed by the film than that in the simulation, thus the simulation over-estimates the scribe width. Additionally, micro cracking and fracture driven mechanical interactions along the substrate film interface may play a significant role in the energy release process. Such mechanisms are not considered in the current model and may result in the partial removal of SnO_2:F film observed in experiments. Lastly, material properties, such as thermal capacity, conductivity and absorption coefficient are assumed constant, non-temperature dependent and homogeneous. The effect of fluorine doping and other impurities are also not considered in the model. These reasons may cause the over-estimation of the simulation results.

The current model is capable of capturing the film removal process. The model shows that the film expands more at the top surface and larger stress is induced due to the different thermal expansion, so that the film starts breaking from top to the bottom, and under a certain condition, partial removal occurs. Moreover, the width of the film removal predicted by the model is close as the experimental result. Both show the trend of decreasing width with decreasing fluence.

4.2 Experiments on Laser Scribing of SnO2:F Thin Films

Glass side laser scribing results are shown in Fig. 8 for a film processed at 127J/cm^2. Optical profilometry results, given in Fig. 8(b), show that the sidewall of the removed area is steep and the scribe is 35μm in width with no positive ridges. It is observed that the scribe depth is slightly greater than the film thickness (400nm) at some locations. This suggests that substrate damage occurs at this fluence. SEM cross-sectional images (Fig. 6(c)), show that the sidewall possesses similar granular structures as the surface of the film. This suggests that no melt material attached on the sidewalls and the entire scribe boundary is removed mechanically rather than through

thermal ablation. Brittle crack propagation, caused by laser-induced plasma, along the transverse direction makes the scribe width much larger than the beam spot size, and the non-thermal-affected sidewalls is formed by the thermal stress. Film removal quality is estimated by atomic density measurement at the removal area via EDX shown in Fig. 6(d). Line scanning EDX shows that there is a little residual tin after one laser pulse irradiation, which may be removed during laser scribing with a certain pulse overlap. Silicon is detected at the undamaged surface because the electron penetration depth of SnO_2:F is ~1.3μ is estimated by [24]

$$X\,(\mu m)=0.1E^{1.5}/\rho \tag{11}$$

where E is accelerating voltage (keV) and ρ is density (g/cm^3). This observation shows a promising manufacturing process – mechanical dominant removal at the boundary, clean scribe with steep sidewalls. Further simulation investigations will consider higher fluence processing regimes with coexisting ablation and thermal stress film removal mechanisms.

As a comparison of the glass-side laser treatment, the film-side laser scribing with a fluence of 127J/cm^2 is carried out. Fig. 9(a) gives the 3D profile of the scribe area. The film is completely removed with a diameter of 50μm. A positive ridge exists around the scribe boundary due to SnO_2:F vapor redeposition. Thermal ablation based film removal process is driven by the thermodynamical phase transition of the film material. During the ablation process, the material is vaporized, and the vapor moves away from the target due to the high pressure. Some vaporized material redeposits on high-temperature areas, specifically the melted material at the scribe boundary, via the vapor-liquid-solid mechanism [25]. Vapor redeposit is characterized by the protruding material around the boundary of the scribe. The sidewall of a scribed processed from the film side is captured in Fig. 9(b). It is seen that the granular structure disappears on the entire sidewall, which covered with the resolidified material instead. The combined effects of the

protruded ridge and residual solidified molten layer on the sidewalls indicate that film-side laser scribing can lead to undesired electrical properties.

A parametric study on glass-side laser scribing is carried out to fully understand the mechanisms under different laser treatment conditions. The scribe width and depth under different laser fluences are shown in Fig. 10. It is observed that the scribe depth increases with increasing fluence until the film is completely removed. This near-linear trend is not observed in the scribe width. Width increases with fluence when treated by the fluences below $20J/cm^2$ and above $60J/cm^2$. When the fluence is between $20J/cm^2$ and $60J/cm^2$, the width remains constant. This observation indicates that a mechanism transition occurs under different fluences. At fluences below $20J/cm^2$, the removal mechanism is mechanically dominant. The thermal stress is induced by the increasing temperature, and thus the scribe depth and width increase with increased fluence. At fluences between 20 and $60J/cm^2$, thermal ablation removal becomes dominant. An area close to the spot size is thermally removed and part of the film is mechanically removed due to thermal stress. At fluences greater than $60J/cm^2$, film surrounding the high-pressure plasma is removed by crack propagation, and the sidewalls are formed mainly by mechanical removal.

Both simulation and experimental show that SnO_2:F film can be removed before the temperature reaches the melting temperature, therefore, if the scribe quality, such as thermal effect and scribe width, is more important than the manufacturing throughput, this thermal-stress dominant film removal can be considered. Otherwise, a mechanical dominant film removal at fluences may be used resulting in clean scribe boundaries and larger scribe widths.

5. Simulation on CdTe Film Removal by Micro-Explosion

Selective scribing of a 2μm thick CdTe film is performed with a green laser at a wavelength of 532nm. A green laser is used because the melting threshold of SnO_2:F is much larger than that of CdTe at this wavelength. Therefore, laser energy can be highly transmitted though the SnO_2:F film, and fully absorbed by the CdTe film within a very thin layer near the CdTe/SnO_2:F interface. The penetration depth of CdTe at 532nm wavelength is around 167nm, which is thinner than the CdTe film thickness (2μm) by one order of magnitude. The high energy density absorbed within the thin CdTe layer increases local temperature above vaporization temperature and induces material ionization, resulting in plasma generation. The plasma is confined by the solid CdTe and SnO_2:F and is under high pressure, which lifts off the solid CdTe film above, resulting in film removal and delamination. This film removal mechanism is known as the micro-explosion process.

As shown in Fig. 11, the model is composed of a 2μm thick CdTe layer is on the top of the 400nm thick SnO_2:F layer and 50μm thick glass substrate. To consider the traction stresses at the CdTe/SnO_2:F interface, a 10nm thick layer of cohesive elements is also implemented at the interface. The cohesive layer is governed by the traction separation law described in Sec. 2.3, and serves the purpose of simulating the process in which the CdTe film lifts up and delaminates from the SnO_2:F layer caused by the plasma expansion. The thermal analysis is carried out with the consideration of energy loss due to the reflection at the interfaces of SnO_2:F/CdTe and glass/ SnO_2:F, as well as the absorption by the glass substrate and SnO_2:F layer. Material properties are shown in Table 1. The Laser pulse duration is 50ns and wavelength is 532nm. The laser energy is given by [6]

$$E(r,z,t) = (1-R_g-A_g)(1-R_t)(1-R_c)\alpha_c I(r,z,t)e^{-\alpha_t T_t}e^{-\alpha_c(z-T_t-T_g)} \quad (12)$$

where R_c and α_c are the reflectivity and absorption coefficient of CdTe, and T_t is the thickness of SnO_2:F. Fig. 11 shows the temperature distribution as a result of the glass-side laser irradiation at a fluence of 0.2Jcm^2. It can be observed that the absorbing volume in the CdTe layer is confined near the CdTe/SnO_2:F interface, rather than uniformly distributed in the SnO_2:F layer as shown in Fig. 2. This highly confined energy increases temperature higher than the vaporization temperature of CdTe (1400K), generating plasma. Fig. 12 shows the temporal distribution of plasma pressure under the fluences from 0.2J/cm^2 to 0.8J/cm^2 as generally used in experiments. The plasma pressure achieves several hundred Mega Pascal which is much larger than the CdTe failure strength.

The pressure with the temporal and spatial pressure distributions described in Sec. 2.2 and Fig. 12 are incorporated and exerted on both CdTe and SnO_2:F layers at the interface. The width of plasma is assumed to be the same as the beam spot size – 10μm. A snapshot of stress distribution in the film and substrate at 10ns after the onset of laser pulse is given in Fig. 13. The CdTe film is pushed upward due to the plasma expansion. This deformation expands the top center of the film in the r direction, generating a S_{11} tensile stress. Stress in the z direction (S_{22}) is much smaller. Therefore, the principal stress on the top center of the film is mainly contributed from the S_{11} tensile stress, as shown in Fig. 13. Similarly, a compressive principal stress exists at the lower part of film center due to CdTe film deformation. At the edge of the plasma, a large principal tensile stress is observed at the CdTe/SnO_2:F interface. This principal tensile stress comes from the traction stress between the SnO_2:F and the deforming CdTe layers. The traction at the interface is considered in more detail in Fig. 14, in which Region A in Fig. 13 in

magnified. It can be seen that large S_{22} stress in the CdTe layer, SnO_2:F layer, and the cohesive elements near the plasma boundary. This S_{22} stress is induced by the deformation of CdTe layer caused by the plasma expansion. The deforming CdTe layer in turn pulls the cohesive elements upwards. Deformed cohesive elements carry a tensile stress governed by the traction separation law, binding the CdTe film to the SnO2:F substrate, and the surrounding CdTe and SnO2:F elements also experience a tensile S_{22} stress. It is observed that S_{22} tensile stress in the film is smaller than S_{11} tensile stress; therefore, S_{11} tensile stress is dominant for the CdTe material removal. As the film deforms, the S_{11} tensile stresses at the top center and plasma boundaries in the film increases, and the film starts breaking at these locations when the principal stress satisfies the Coulomb-Mohr criterion.

A snapshot at the early stage of the film breaking taken at 20ns is given in Fig. 15, which shows that material failure initiates at the center. The removal of the CdTe elements on the top center of the film is the tensile stresses dominant removal, while removal of the elements on the bottom center is dominant by the compressive stresses. Some elements near the plasma boundaries are removed due to the large S_{22} tensile stress caused by the confinement between the cohesive elements and CdTe material. Cohesive elements failed and are deleted from the calculation based on the traction separation analysis, initiating film delamination. Material failure and film delamination both contribute to the film removal at this stage. In order to capture the processes of film breaking, the stress evolution of the failed elements at the top center and bottom center of the CdTe layer is shown in Fig. 16. The element at the top center sees tensile stress (maximum principal stress) during the simulation and is responsible for the film removal. The element at the bottom center sees compressive stress (minimum principal stress). Stresses carried in both elements increase with simulation time before failure. Once the Coulomb-Mohr criterion is met,

the element fails and no longer carries stresses. The greater compressive failure strength causes the delay of material failure at the bottom center, which indicates that film breaking initiates from the top center to the bottom.

Fig. 17 gives the typical evolution of stresses and the quadratic nominal stress ratio defined in Eq. (7) of a removed cohesive element. The nodal displacement of the cohesive element, which represents the displacement of the deforming film before element failure, is also shown. In the early stage the plasma pressure lifts the CdTe film upwards, and the cohesive element experiences S_{22} tensile stress, while the shear stress S_{12} is less dominant. The quadratic nominal stress ratio is the criterion to determine the initiation of cohesive element damage. Once the ratio reaches 1, damage initiates and the stress to be carried begins to reduce. The cohesive element then undergoes a large deformation, mainly in the z direction. Once the nodal displacement reaches a predefined value, traction stress becomes zero and the cohesive element is removed from the calculation. This suggests no confinement between the film and substrate; film delamination then occurs. The late stage of the micro-explosion process is shown in Fig. 18. As CdTe layer keeps deforming, it also begins breaking into multiple segments due to brittle failure. At the same time, the width of the removed film keeps enlarging from 10μm (assumed initiated size of the plasma) to 12.5μm. The enlarged opening shows a scribe width of 2.5μm. Complete film removal is achieved. The simulation shows that the film removal process via the micro-explosion mechanism is contributed from both brittle failure and film delamination processes without thermal effects. A similar observation of laser scribing of ZnO film on glass substrate is presented by Matylitsky, et al. [12]. The micro-explosion model is capable of predicting the film removal quality of low-penetration-depth materials (compared to the film thickness).

5. Conclusion

Predictive numerical finite element models are demonstrated for glass-side laser scribing of SnO_2:F and CdTe films. A fully-coupled thermal-mechanical model is implemented, showing that SnO_2:F film is removed at a laser fluence below the damage threshold due to thermal stresses. The scribe size is predicted by simulation and is on the same order of magnitude as experimental results. Experimental results also show that SnO_2:F film removal starts from the top, as predicted by the simulation. The micro-explosion model is developed for glass-side laser scribing of CdTe films, with the stress loading estimated by the laser-induced plasma pressure. A CdTe removal process dominated by both brittle failure and delamination with reduced thermal effects, as captured by the numerical model, is desired for reducing scribing dead zones and interlaminar shorts. Such a process is highly desirable for improved scribe quality and greater process efficiency. Numerical models investigated in this work are capable of predicting the material removal dynamics and fracture behavior of SnO_2:F and CdTe. Further numerical developments are aimed at predictively modeling the scribing line profile by taking account of the laser pulse overlapping.

Acknowledgments

The use of material characterization equipment at Material Research Science and Engineering Center, Columbia University is gratefully acknowledged. The authors also would like to thank Pilkington North America Inc. for providing SnO_2:F coated samples.

References

[1] R.G. Dhere, M. Bonnet-Eymard, E. Charlet, E. Peter, J.N. Duenow, J.V. Li, D. Kuciauskas, T.A. Gessert, CdTe solar cell with industrial Al:ZnO on soda-lime glass, Thin Solid Films, 519 (2011) 7142-7145.

[2] A. Luque, S. Hegedus, Handbook of Photovoltaic Science and Engineering, Wiley, UK, 2003.

[3] H. Booth, Laser processing in industrial solar module manufacturing, Journal of Laser Micro/Nanoengineering, 5 (2010) 183-191.

[4] A.D. Compaan, S.N. Matulionis, Laser scribing of polycrystalline thin films, Opt. Lasers Eng. 34 (2000) 15-45.

[5] R. Murison, C. Dunsky, M. Rekow, C. Dinkel, J. Pern, L. Mansfield, T. Panarello, S. Nikumb, CIGS P1, P2 and P3 laser scribing with an innovative fiber laser, 35th IEEE Photovoltaic Specialists Conf. (2010) 179-184.

[6] J. Bovatsek, A. Tamhankar, R.S. Patel, N.M. Bulgakova, J. Bonse, Thin film removal mechanisms in ns-laser processing of photovoltaic materials, Thin Solid Films 518 (2010) 2897-2904.

[7] P. Gecys, G. Raciukaitis, Scribing of a-Si thin film solar cells with picoseconds laser, Eur. Phys. J. Appl. Phys. 51 (2010) 33209.

[8] C.M. Dunsky, F. Colville, Scribing thin-film solar panels, Industrial Laser Solutions for Manufacturing (2008).

[9] W. Wang, K.D. Wang, G.D. Jiang, X.S. Mei, C.J. Yang, Comparison of femtosecond laser-induced front- and rear-side ablation of films, Proc. Inst. Mech. Eng., Part B: J. Eng. Manuf. 225 (2010) 520-527.

[10] S. Beyer, V. Tonrnari, D. Gornicki, Comparison of laser induced front- and rear side ablation, Proc. SPIE 5063 (2003) 202-207.

[11] T. Sano, H. Yamada, T. Nakayama, I. Miyamoto, Laser induced rear ablation of metal thin films, Proc. SPIE 4426 (2002) 70-73.

[12] V.V. Matylitsky, H. Huber, D. Kopf, Selective removal of transparent conductive oxide layers with ultrashort laser pulses: front- vs. back-side ablation, Int. Congr. App. Lasers Electro-Opt. M903 (2011) 1022-1027.

[13] W. Shinohara, M. Shima, S. Taira, K. Uchihashi, A. Terakawa, Applications of laser patterning to fabricate innovative thin-film silicon solar cells, Proceedings of SPIE (2006) 6107.

[14] M. Kontgers, I. Kunze, S. Kajari-Schroder, X. Breitenmoser, B. Bjorneklett, Quantifying the risk of power loss in PV modules due to micro cracks, 25th European Photovoltaic Solar Energy Conference, Valencia, Spain (2010).

[15] M.V. Seica, J.A. Packer, Mechanical properties and strength of aged cast iron water pipes, Journal of Materials in Civil Engineering, 16 (2004) 69-77.

[16] R. Fabbro, J. Fournier, P. Ballard, D. Devaux, J. Virmont, Physical study of laser-produced plasma in confined geometry, J. Appl. Phys. 68 (1990) 775-784.

[17] W. Zhang, Y.L. Yao, Micro-scale laser shock processing of metallic components, ASME Trans. J. Manuf. Sci. Eng., 124 (2002) 369-378.

[18] G.M. Carlomagno, C.A. Brebbia, Computational Methods and Experimental Measurements XV, WIT Press, Southampton, 2011.

[19] P.P. Camanho, C.G. Dávila, Mixed-mode decohesion finite elements for the simulation of delamination in composite materials, NASA Langley Res. Cent. TM-2002-211737 (2002) 1-37.

[20] C. Peter, Properties of Narrow Gap Cadmium-Based Compounds, the Institution of Electrical Engineers, UK, 1994.

[21] A. Luque, S. Hegedus, Handbook of Photovoltaic Science and Engineering, second ed., John Wiley & Sons, UK, 2011.

[22] J.R. Assay, M. Shahipoor, High-Pressure Shock Compression of Solids, Springer-Verlag, New York, 1992.

[23] M. Rubin, Optical constants and bulk optical properties of soda lime silica glasses for windows, Sol. Energy Mater. 12 (1985) 275-288.

[24] P.J. Potts, A Handbook of Silicate Rock Analysis, Chapman and Hall, London, UK, 1987.

[25] D.H. Lowndes, J.D. Fowlkes, A.J. Pedraza, Early stage of pulsed-laser growth of silicon microcolumns and microcones in air and SF_6, Appl. Surf. Sci. 154-155 (2000) 647-658.

List of Table Captions

List of Figure Captions

Fig. 1. Illustration of the glass-side laser scribing model for SnO_2:F and CdTe film removal. Lasers with wavelength of 1064nm and 532nm are adopted for SnO_2:F and CdTe scribing, respectively.

Fig. 2. Temperature distribution in the SnO_2:F/glass multilayer system under laser irradiation at a fluence of 3J/cm^2. A large penetration depth of laser energy allows for a uniform temperature distribution along film thickness. Snapshot is taken at 36ns. 10X Deformation scale for viewing clarity.

Fig. 3. Fully coupled thermal stress analysis of SnO_2:F removal by laser irradiation at a fluence of 3J/cm^2 at 38ns. Absorption of laser energy induces local thermal expansion and thermal stress. Elements experiencing a principal stresses larger than the failure strength are deleted from calculation. A 2μm opening has been generated accordingly. 10X Deformation scale for viewing clarity.

Fig. 4. Principal stress and heat flux history in an element at SnO_2:F film center. The element deletion occurs at 38ns. Heat flux drops to zero due to instantaneous dependence between thermal and mechanical analyses.

Fig. 5. The result of SnO_2:F removal by 3J/cm^2 laser irradiation based on the fully coupled thermal stress analysis. An 8.3μm opening is generated. The snapshot is taken at 200ns. Deformation scale is 10X for viewing clarity.

Fig. 6. Temperature and stress history in a deleted element at SnO_2:F film center treated at a fluence of 1J/cm^2. The element is subjected to a compressive stress followed by a tensile stress. The element fails when the tensile failure stress is met at 1430ns.

Fig. 7. Comparison of depths and widths of the removed SnO_2:F films obtained in simulation and experiments. The film is completely removed in depth for all the conditions used in the simulations.

Fig. 8. (a) SEM image of the film removal by single pulse processed SnO_2:F samples from glass side at a fluence of 127J/cm^2; (b) Removal line profile along A measured by optical profilometry; (c) SEM image of scribe sidewall; (d) EDX line profile scanning along A.

Fig. 9. (a) 3D scanning of the removal film profile by optical profilometry and (b) SEM image of the sidewall of film removal by single pulse processed SnO_2:F samples from film side at a fluence of 127J/cm^2.

Fig. 10. Dependence of removal depth and width on laser fluence. Error bars indicate standard deviation.

Fig. 11. Temperature distribution of CdTe/SnO_2:F/glass multilayer system under laser irradiation at a fluence of 0.2J/cm^2.

Fig. 12. Temporal distribution of the plasma pressure at different fluences from 0.2J/cm^2 to 0.8J/cm^2.

Fig. 13. Micro-explosion model with a pressure input at the CdTe/SnO2:F interface and the plasma dimension is 10μm in width. A layer of cohesive elements is defined between the CdTe layer and SnO_2:F layer. The CdTe film deforms due to the plasma expansion. The snapshot is taken at 10ns. Deformation scale is 10X for viewing clarity.

Fig. 14. S_{22} stress distribution of the magnified area A in Fig. 11 at the same moment. The cohesive elements have been deformed due to S_{22} stress. Deformation scale is 10X for viewing clarity.

Fig. 15. S_{22} stress distribution of the region shown in Fig. 12 at the later stage (20ns), showing some cohesive elements have been deleted. Deformation scale is 10X for viewing clarity.

Fig. 16. Stress evolution of the failed elements at the top center and bottom center of the CdTe layer. Tensile stress occurs on the top, while compressive stress occurs at the bottom. The stresses drop to zero once the Coulomb-Mohr criterion is met.

Fig. 17. Typical evolution of stresses and the quadratic nominal stress ratio defined in Eq. (7) of the removed cohesive elements. Nodal displacement of the cohesive element is also shown.

Fig. 18. Maximum principal stress distribution at 66ns. The film has been completely removed with an opening width of 12.5μm. Both brittle failure and film delamination contribute to the film removal. Deformation scale is 2X for viewing clarity.

Table 1. Material properties used in simulation.

Properties	Unit	CdTe	SnO_2:F	Glass
Density, ρ	g/cm^3	5.85	6.95	2.52
Conductivity, k	W/mK	6.2	3.2	1
Latent Heat, L	10^5J/kg	2.092	3.17	--
Spec. Heat, C_P	J/kgK	210	353	800
Exp. Coef., κ	10^{-6}/K	5.9	4	8.6
Modulus, E	GPa	52	401	72
Poisson ratio, v		0.41	0.291	0.22
Refractive index @1064nm		--	1.6+i0.05	$1.51+i5.0\times10^{-6}$
Refractive index @532nm		2.72+i0.286	1.98+i0.01	$1.53+i1.8\times10^{-7}$
Melt. Temp., T_m	K	1370	1903	1873
Vap. Temp., T_v	K	1403	2123	--
Impedance, Z	$10^7kg/m^2s$	1.8	--	1.21
Tensile failure strength	MPa	40	500	--
References		[20-22]	[6,21]	[6, 21-23]

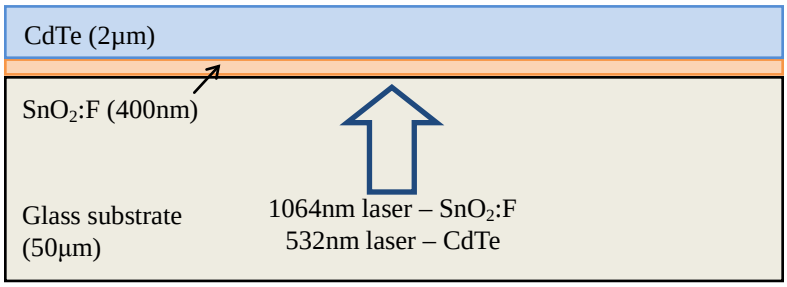

Fig. 1. Illustration of glass-side laser scribing model for SnO_2:F and CdTe film removal. Lasers with wavelength of 1064nm and 532nm are adopted for SnO_2:F and CdTe scribing, respectively.

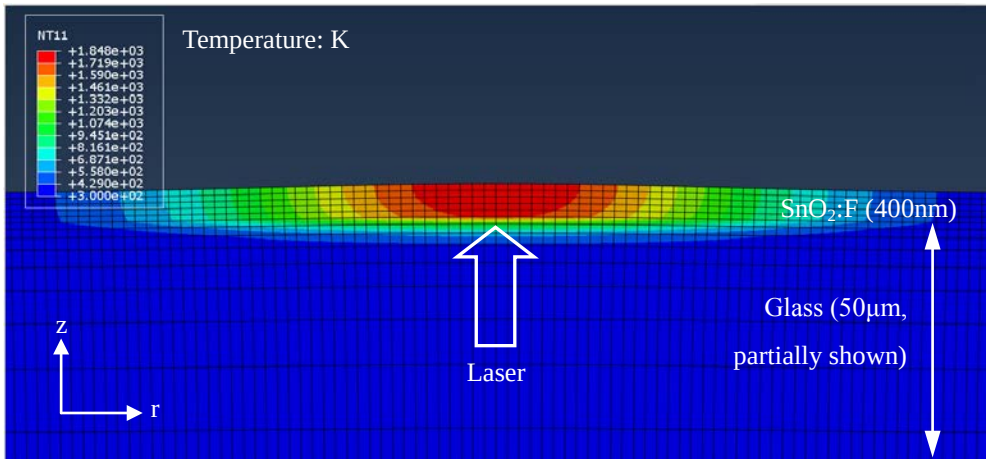

Fig. 2. Temperature distribution in the SnO_2:F/glass multilayer system under laser irradiation at a fluence of 3J/cm^2. A large penetration depth of laser energy allows for a uniform temperature distribution along film thickness. Snapshot is taken at 36ns. 10X Deformation scale for viewing clarity.

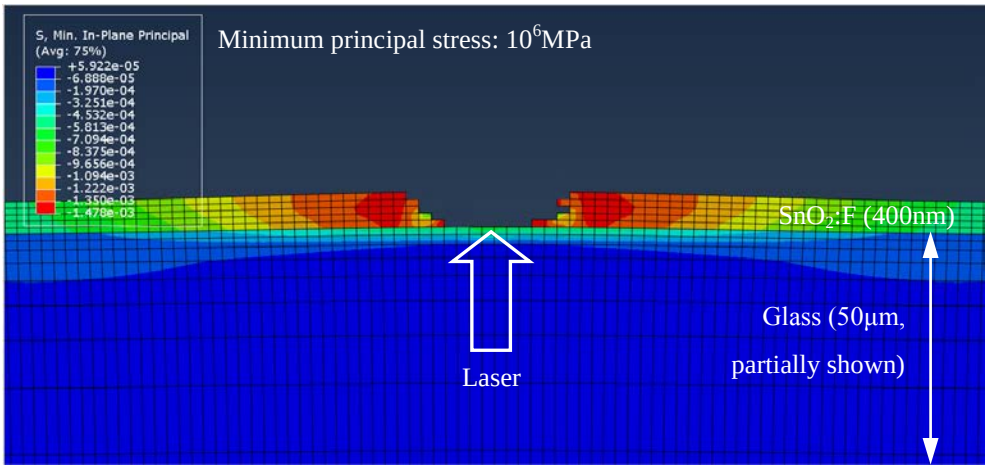

Fig. 3. Fully coupled thermal stress analysis of SnO_2:F removal by laser irradiation at a fluence of 3J/cm^2 at 38ns. Absorption of laser energy induces local thermal expansion and thermal stress. Elements experiencing a principal stresses larger than the failure strength are deleted from calculation. A 2μm opening has been generated accordingly. 10X Deformation scale for viewing clarity.

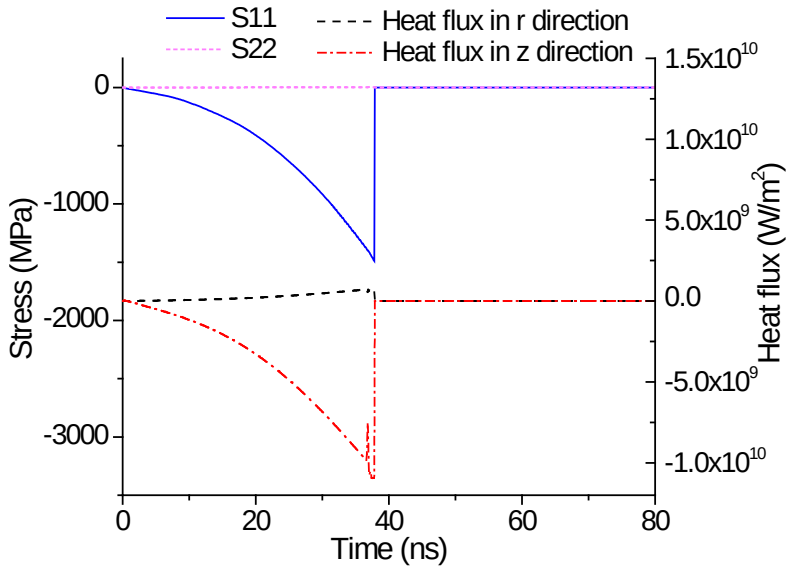

Fig. 4. Stress and heat flux history in an element at SnO_2:F film center. The element deletion occurs at 38ns. Heat flux drops to zero due to instantaneous dependence between thermal and mechanical analyses.

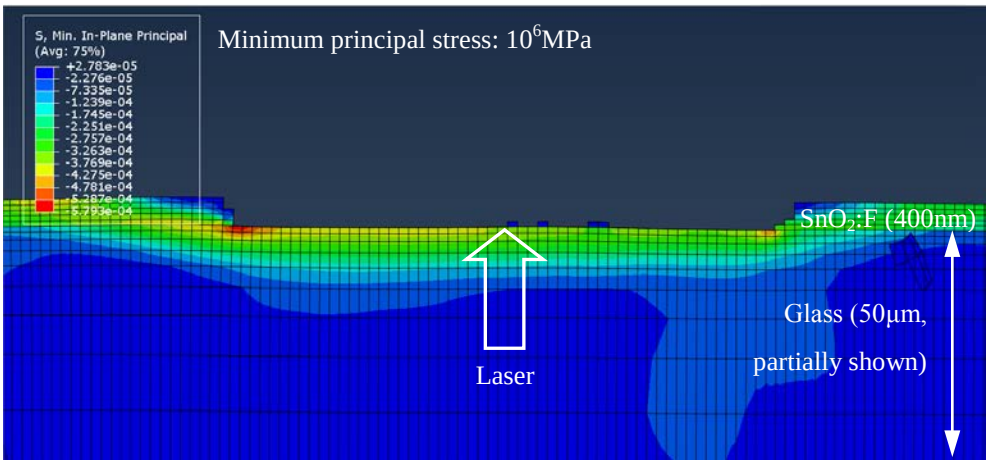

Fig. 5. The result of SnO_2:F removal by 3J/cm^2 laser irradiation based on the fully coupled thermal stress analysis. An 8.3μm opening is generated. The snapshot is taken at 200ns. Deformation scale is 10X for viewing clarity.

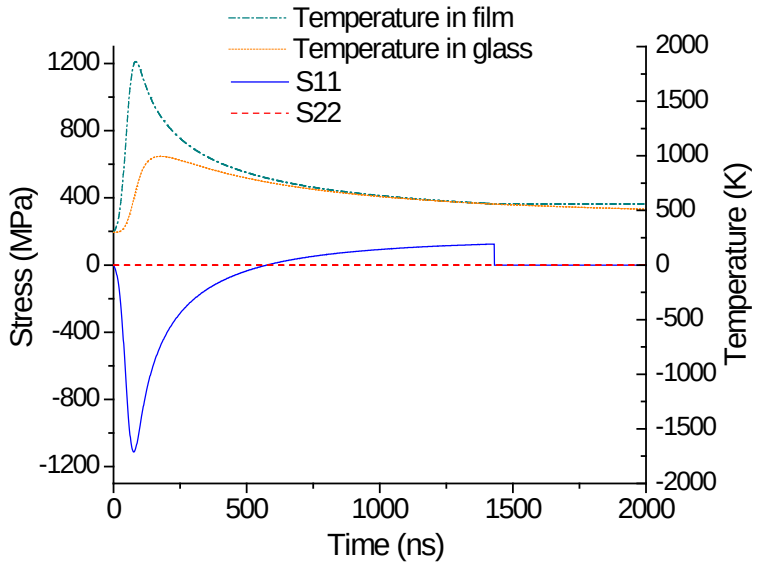

Fig. 6. Temperature and stress history in a deleted element at SnO_2:F film center treated at a fluence of 1J/cm^2. The element is subjected to a compressive stress followed by a tensile stress. The element fails when the tensile failure stress is met at 1430ns.

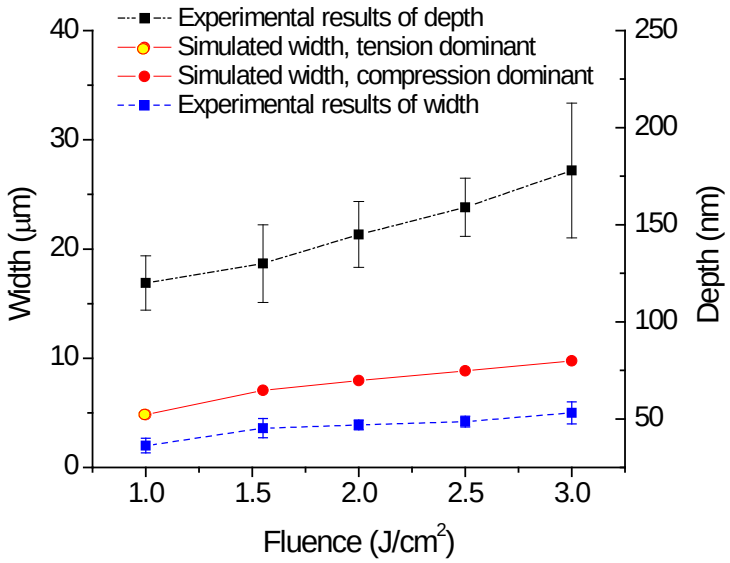

Fig. 7. Comparison of depths and widths of the removed SnO_2:F films obtained in simulation and experiments. The film is completely removed in depth for all the conditions used in the simulations.

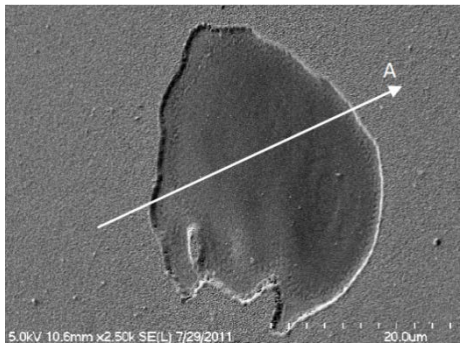

(a) Overview of film removal

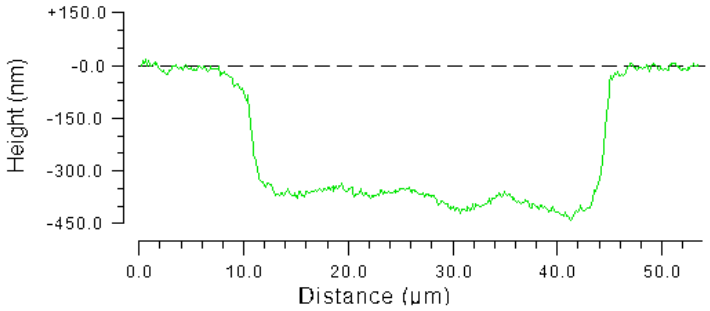

(b) Optical profilometry measurement

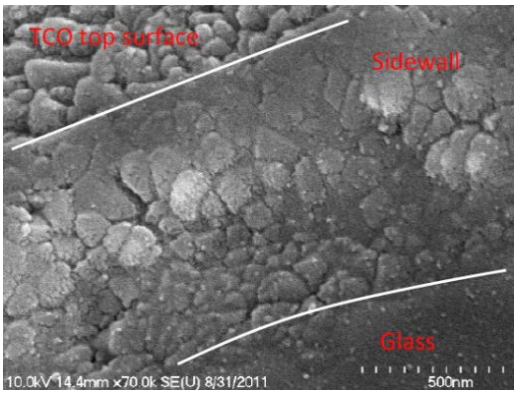

(c) Sidewall of the film removal

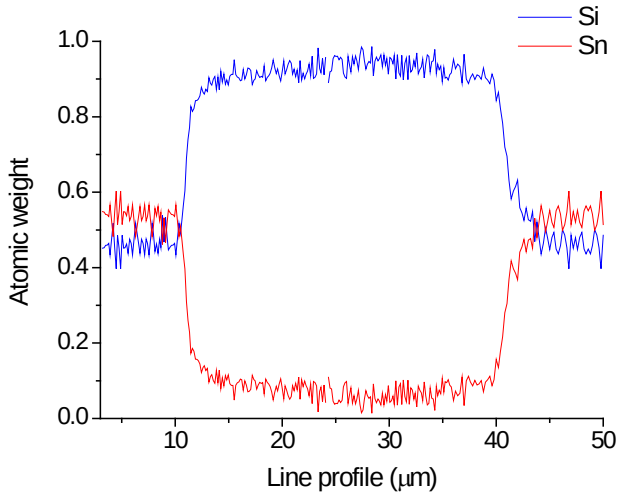

(d) EDX line scan profile

Fig. 8. (a) SEM image of the film removal by single pulse processed SnO_2:F samples from glass side at a fluence of 127J/cm^2; (b) Removal line profile along A measured by optical profilometry; (c) SEM image of scribe sidewall; (d) EDX line profile scanning along A.

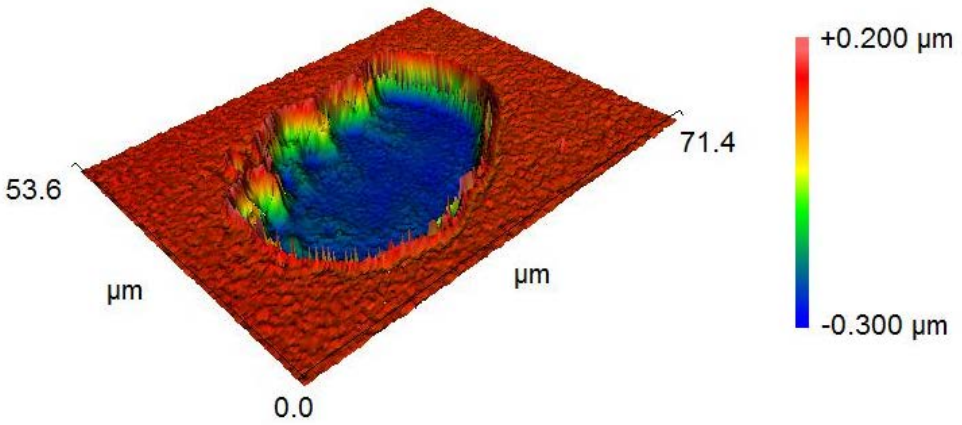

(a) 3D scan profile by optical profilometry

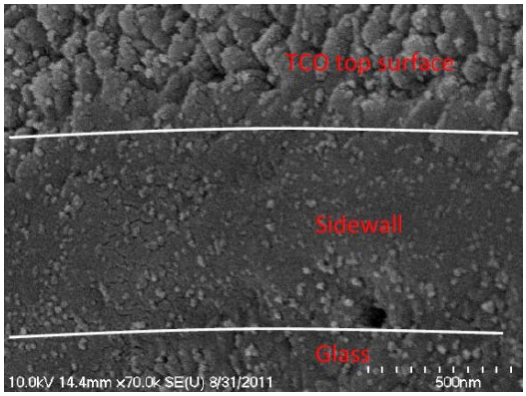

(b) Sidewall of the film removal

Fig. 9. (a) 3D scanning of the removal film profile by optical profilometry and (b) SEM image of the sidewall of film removal by single pulse processed SnO_2:F samples from film side at a fluence of 127J/cm^2.

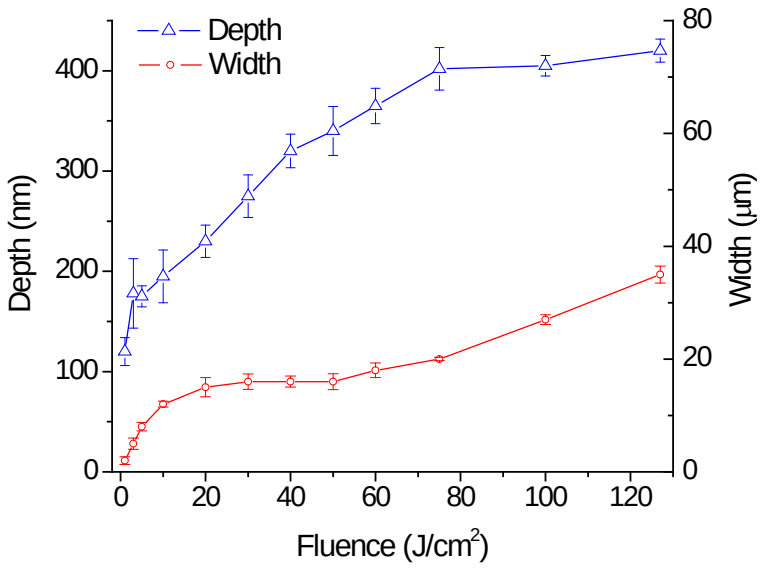

Fig. 10. Dependence of removal depth and width on laser fluence. Error bars indicate standard deviation.

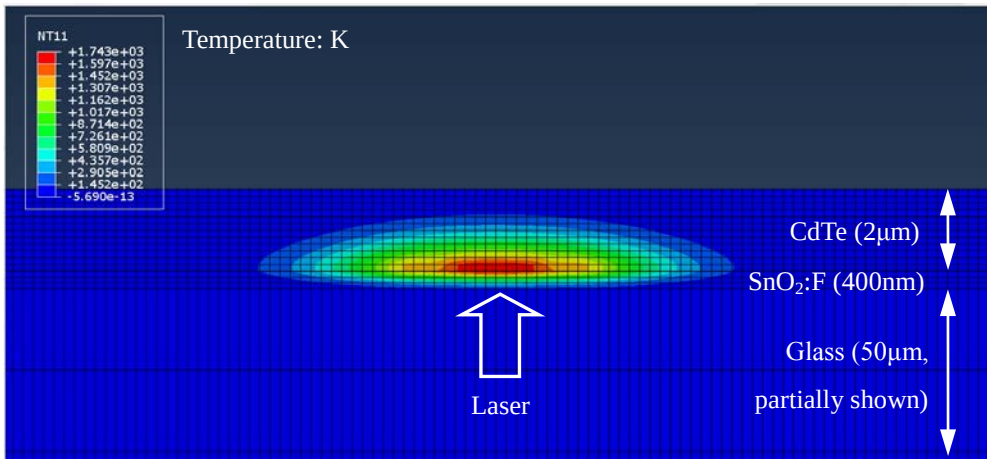

Fig. 11. Temperature distribution of CdTe/SnO_2:F/glass multilayer system under laser irradiation at a fluence of 0.2J/cm^2.

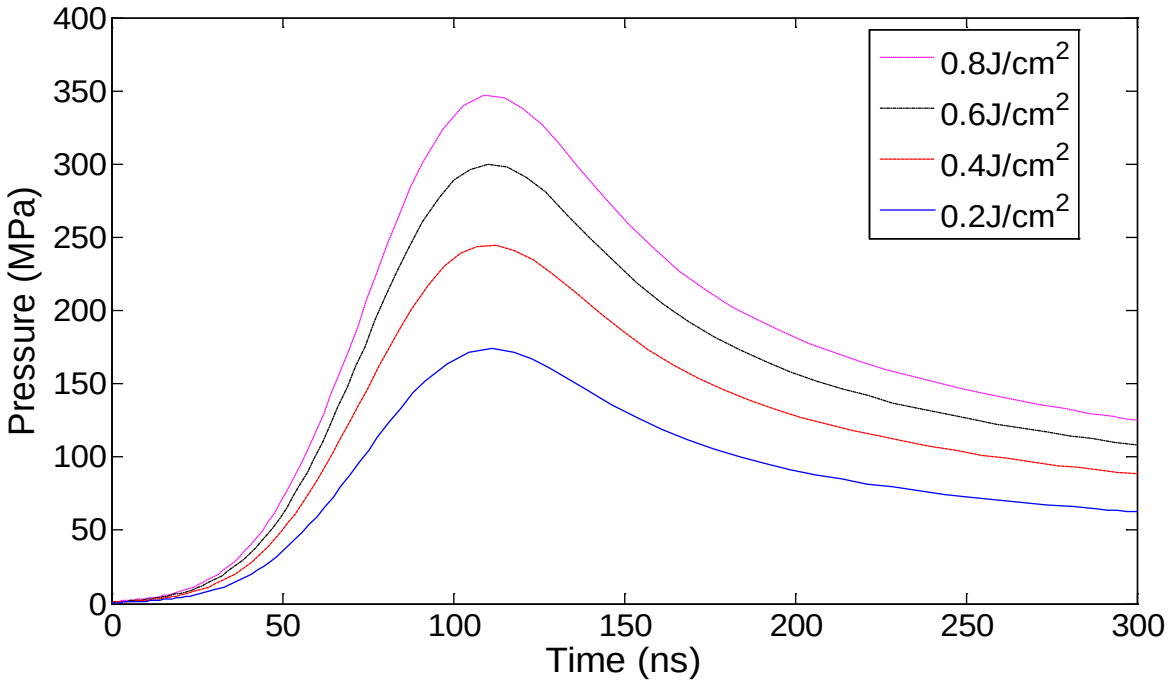

Fig. 12. Temporal distribution of the plasma pressure at different fluences from 0.2J/cm^2 to 0.8J/cm^2.

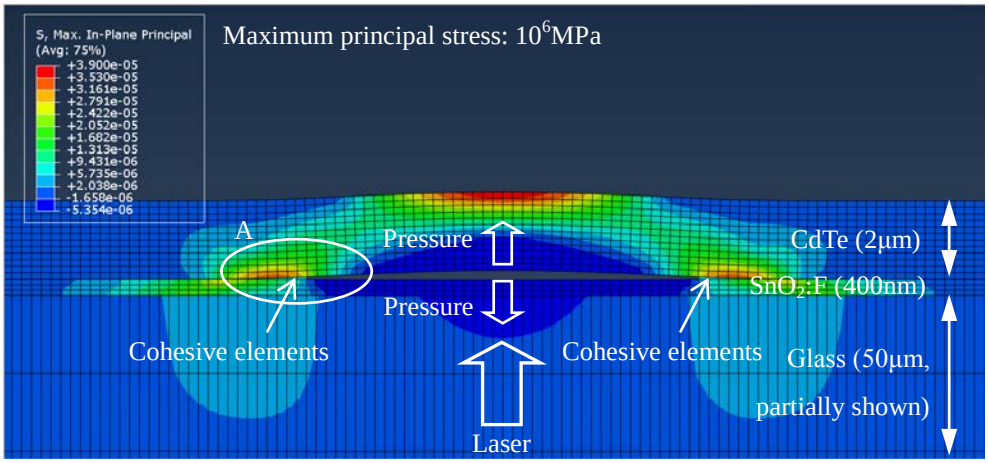

Fig. 13. Micro-explosion model with a pressure input at the CdTe/SnO2:F interface and the plasma dimension is 10μm in width. A layer of cohesive elements is defined between the CdTe layer and SnO_2:F layer. The CdTe film deforms due to the plasma expansion. The snapshot is taken at 10ns. Deformation scale is 10X for viewing clarity.

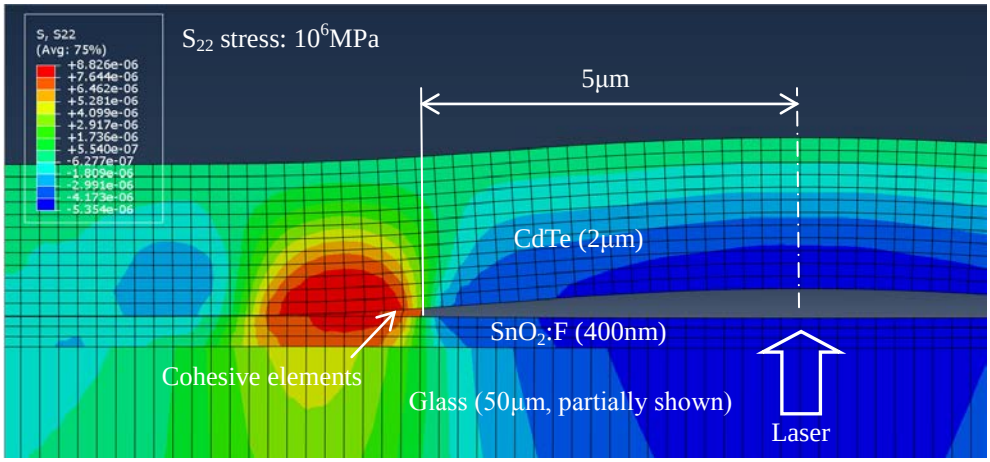

Fig. 14. S_{22} stress distribution of the magnified area A in Fig. 11 at the same moment. The cohesive elements have been deformed due to S_{22} stress. Deformation scale is 10X for viewing clarity.

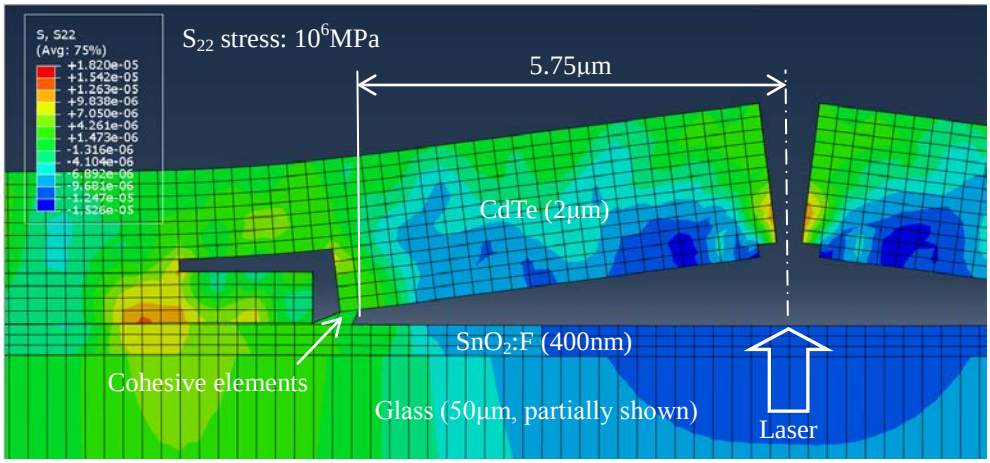

Fig. 15. S_{22} stress distribution of the region shown in Fig. 12 at the later stage (20ns), showing some cohesive elements have been deleted. Deformation scale is 10X for viewing clarity.

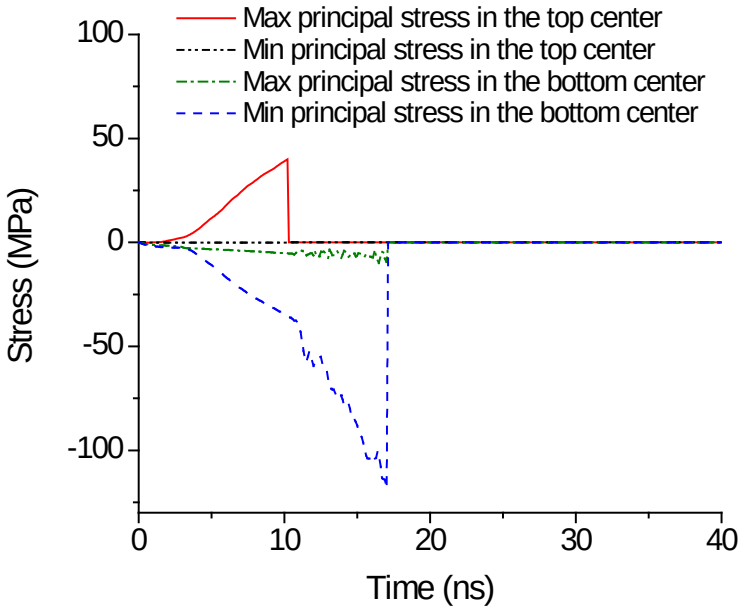

Fig. 16. Stress evolution of the failed elements at the top center and bottom center of the CdTe layer. Tensile stress occurs on the top, while compressive stress occurs at the bottom. The stresses drop to zero once the Coulomb-Mohr criterion is met.

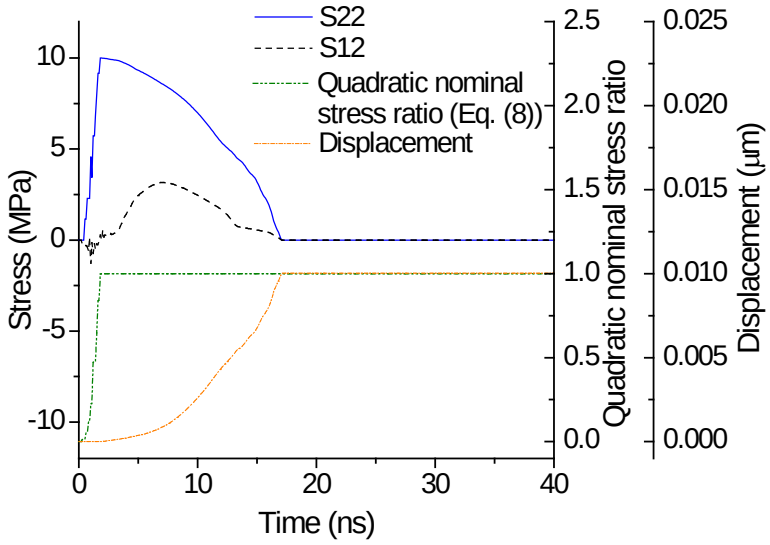

Fig. 17. Typical evolution of stresses and the quadratic nominal stress ratio defined in Eq. (7) of the removed cohesive elements. Nodal displacement of the cohesive element is also shown.

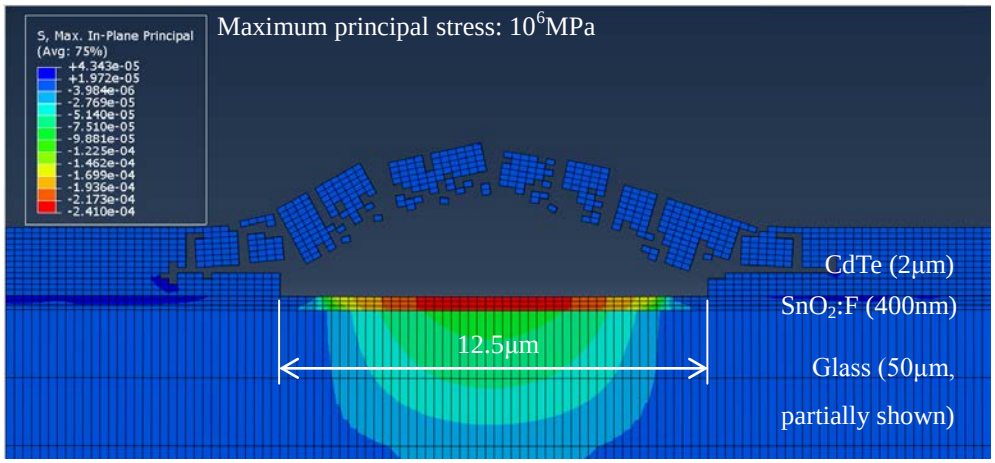

Fig. 18. Maximum principal stress distribution at 66ns. The film has been completely removed with an opening width of 12.5μm. Both brittle failure and film delamination contribute to the film removal. Deformation scale is 2X for viewing clarity.